

Northumbria Research Link

Citation: Winter, Kate, Lombardi, Denis, Diaz-Moreno, Alejandro and Bainbridge, Rupert (2021) Monitoring Icequakes in East Antarctica with the Raspberry Shake. *Seismological Research Letters*, 92 (5). pp. 2736-2747. ISSN 0895-0695

Published by: Seismological Society of America

URL: <https://doi.org/10.1785/0220200483> <<https://doi.org/10.1785/0220200483>>

This version was downloaded from Northumbria Research Link:
<http://nrl.northumbria.ac.uk/id/eprint/45986/>

Northumbria University has developed Northumbria Research Link (NRL) to enable users to access the University's research output. Copyright © and moral rights for items on NRL are retained by the individual author(s) and/or other copyright owners. Single copies of full items can be reproduced, displayed or performed, and given to third parties in any format or medium for personal research or study, educational, or not-for-profit purposes without prior permission or charge, provided the authors, title and full bibliographic details are given, as well as a hyperlink and/or URL to the original metadata page. The content must not be changed in any way. Full items must not be sold commercially in any format or medium without formal permission of the copyright holder. The full policy is available online: <http://nrl.northumbria.ac.uk/policies.html>

This document may differ from the final, published version of the research and has been made available online in accordance with publisher policies. To read and/or cite from the published version of the research, please visit the publisher's website (a subscription may be required.)

1 **Monitoring icequakes in East Antarctica with the Raspberry Shake**

2

3 Kate Winter, Denis Lombardi, Alejandro Diaz-Moreno, Rupert Bainbridge

4

5 **Declaration of Competing Interests**

6 The authors acknowledge there are no conflicts of interest recorded.

7 **Monitoring icequakes in East Antarctica with the Raspberry Shake**

8

9 **Authors:** Kate Winter^{1*}, Denis Lombardi², Alejandro Diaz Moreno^{3,4}, Rupert Bainbridge⁴

10

11 **Author Affiliations**

12 ¹Department of Geography and Environmental Sciences, Engineering and Environment,
13 Northumbria University, Newcastle upon Tyne, UK.

14 ²Independent Researcher, 05 rue Jussieu, 75005 Paris, France.

15 ³Reynolds International Ltd, Suite 2, Broncoed House, Broncoed Business Park, Wrexham
16 Road, Mold, Flintshire, UK.

17 ⁴School of Geography, Politics and Sociology, Newcastle University, Newcastle upon Tyne,
18 UK.

19 *Corresponding author: Kate Winter (k.winter@northumbria.ac.uk).

20

21 **Abstract**

22 We evaluate the performance of the low-cost seismic sensor Raspberry Shake (RS) to identify
23 and monitor icequakes (which occur when glacial ice experiences brittle deformation) in
24 extreme environments. In January 2020, three RS3D sensors were installed on a katabatic
25 wind-scoured blue ice area (BIA) close to the Princess Elisabeth Antarctica research station in
26 Dronning Maud Land, East Antarctica. The sensors were configured for Antarctic deployment
27 and placed in insulated enclosures to protect them from harsh weather systems. The RS network
28 (installed in a triangular array) performed well in the cold and with rapid air temperature
29 change, as diurnal temperatures fluctuated from a high of 0.0°C to a minimum temperature of
30 -15.0°C. Although battery connectivity issues in one unit limit full triangulation of seismic
31 signals, and high background noise may mask some seismic signals, data from the RS2 unit

32 reveals that 2936 icequakes were detected over a 10-day period. The temporal occurrence of
33 these icequakes, combined with satellite-derived surface temperature measurements and
34 automatic weather station data, suggest that diurnal fluctuations in solar radiation control ice
35 surface temperature changes, driving thermal contraction of the ice. Seismic investigations like
36 these can therefore provide information on the thermal state and ice fracture mechanics of
37 ablation zones such as BIAs. Our work highlights the potential application of the RS (after
38 minimal modification) in glaciated environments where equipment often needs to be portable,
39 temporary and lightweight, and able to perform in extreme weather conditions.

40

41 **Key words/terms:** Seismology, seismic sensor, blue ice, ice temperature, ice fracture,
42 Antarctica, glaciology

43

44 **Introduction**

45 The Raspberry Shake (RS) is a plug-and-go seismic sensor comprising geophone(s), digitizers,
46 and a Raspberry-Pi computer board. Originally developed in 2016 as a citizen science tool for
47 hobbyists and educators interested in earthquake detection, the RS network has thousands of
48 installations live-streaming seismic data from over 50 countries, in every continent except
49 Antarctica. Because the RS seismic sensors are relatively new, academic publications that
50 document and utilize the technology are limited. Publications are centered around the education
51 and outreach value of the RS (Calais et al., 2020; Diaz et al., 2020; Jeddi et al., 2020; Subedi
52 et al., 2020), as well as the network's potential to complement existing broadband (BB) seismic
53 station data (Anthony et al., 2019; Lecocq et al., 2020). In the Earth Sciences, RS devices have
54 been used to detect rock wall failure and local earthquakes. Both Manconi et al. (2018) and
55 Taruselli et al. (2019) note that RS devices can be a useful monitoring tool for recording the
56 magnitude and frequency of rock wall failure, whereas Anthony et al. (2019) reported that RS

57 units can be used in the Earth Sciences to densify pre-existing earthquake monitoring networks.
58 As the high cost, telecommunications availability, power usage, and resource-intense
59 maintenance of traditional BB seismic stations can restrict the number of seismological
60 investigations, particularly in remote locations, low-cost seismic solutions are becoming
61 increasingly attractive to the scientific community in their bid to densify seismic networks and
62 examine local seismicity (Cochran, 2018). In this article, we evaluate the performance of the
63 low-cost RS seismic sensor through a short-term pilot study of surface icequakes in one of the
64 world's most extreme environments: Antarctica. Local BB data are used for comparison and
65 validation. We combine our seismologic data sets with local automatic weather station (AWS)
66 data and Landsat-8 at-sensor brightness measurements to explore the potential link between
67 temperature and ice fracture mechanics in Antarctic blue ice ablation zones.

68

69 **Study Site**

70 In January 2020, we took three RS3D v5 units (each comprising three Sunfull PS-4.5B
71 geophones) to Dronning Maud Land, East Antarctica, where temperatures seldom rise above
72 0°C and winds sometimes gust up to 90 km/hr. To assess the performance of the RS in detecting
73 icequakes in this extreme environment, the seismic array was set up on a wind-scoured blue
74 ice area (BIA), ~180 km inland of the Roi Baudouin Ice Shelf and 4.4 km west of the summer
75 inhabited Princess Elisabeth Antarctica (PEA) research station (71.94° S, 23.34° E) (Fig. 1).
76 BIAs, which form when katabatic winds scour and ablate the ice surface (Bintanja and van den
77 Broeke, 1995; Bintanja, 1999), cover between 120; 000–241; 000 km² of the ice surface in
78 Antarctica (~0.8%–1.6% of the Antarctic continent (Winther et al., 2001), where they are
79 frequently situated on the leeward side of mountains and mountain ranges. The BIA at our
80 study site is situated at such a location, on the leeward side of the Sør Rondane Mountains, a
81 170-km-long mountain chain, reaching 2–3 km above sea level, which protrudes ~0.2–1.2 km

82 above the East Antarctic Ice Sheet (EAIS, Fig. 1). At the study site, ice flow is very slow (<2
83 ma^{-1} ; Pattyn et al., 2010; Mouginit et al., 2019), presumably because of the absence of a nearby
84 outlet glacier or ice stream. Despite these low-flow speeds, over a thousand icequake signals
85 were recorded in this area by a local permanent BB seismometer (station code: ELIS) - which
86 is situated 4.5 km away from the study BIA (Fig. 1) - over a one-year period (between February
87 2012 and January 2013) (Lombardi et al., 2019). The BB seismometer, a Nanometrics T120
88 PA seismometer characterized by a flat response within the 120 s to 100 Hz band, with a 24-
89 bit digitizer sampling at 100 Hz (connected to Global Positioning System [GPS] and linked to
90 the internet via PEA's satellite connection), is installed within a protective casing and
91 insulating shelter on a granitic ridge outcropping a few meters above the ice surface, 350 m
92 north of PEA (71.9460° S, 23.3467° E). Lombardi et al. (2019) suggested that the icequakes
93 recorded by the BB seismometer are the result of local ice surface contraction, associated with
94 diurnal changes in temperature, linked to solar radiation. Investigations on such thermally
95 induced icequakes can therefore provide indirect information on superficial ice and snow
96 mechanics, as well as the thermal state of the ice sheet (Nishio, 1983; Lombardi et al., 2019),
97 ice shelf (MacAyeal et al., 2019; Olinger et al., 2019), or mountain glacier (Podolskiy et al.,
98 2018; Zhang et al., 2019). In our study, we compare in situ RS data to the local BB station data
99 to assess the ability of the RS to detect local high-frequency seismic activity in glaciated
100 environments.

101

102 **Methods**

103 *Raspberry Shake seismometer*

104 RS seismometers are deployed in a number of environments, but they have yet to be tested in
105 the harsh climate of Antarctica. In this study, we deployed RS3D turn-key seismometers. The

106 RS3D comprises three Sunfull PS-4.5B geophones (one vertical and two horizontal), with a
107 period electronically extended to 2 s, connected to digitizers sampling at 100 Hz and a
108 Raspberry-Pi computer board: all housed in a plastic enclosure. The enclosure has access points
109 to enable power connectivity, SD card change, USB access, and ethernet connectivity.
110 Although the system is designed to be plug-and-play, the Raspberry-Pi component means some
111 parameters can be modified via Linux command line to suit user requirements. For the RS
112 Antarctic deployment, the standard 8 GB micro SD card was replaced with a 32 GB micro SD
113 card to ensure sufficient data storage. Because space is needed for the basic RS image and the
114 estimated data per geophone channel is $\sim 10\text{--}20$ MB per day (although this varies with user
115 settings), this deliberately large increase in storage capacity was a precaution, in case of delays
116 in instrument retrieval and data download. Pre-programmed RS3D settings are designed to
117 store data locally over a seven-day rolling window, with real-time update to the RS servers.
118 With no internet connectivity at our field site for data upload, we set the data storage time to
119 365 days to ensure data would not be overwritten. This is longer than necessary but allowed
120 for extra instrument retrieval time. Should data have been recorded for 365 days, our
121 deployment would be expected to generate 15–20 GB of data. Again, with no internet
122 connectivity, network time protocols would not keep the RS time synchronized, so the starting
123 time was set manually and an internal clock drift of 0.16, 0.39, and 0.50 s/day for the three RS
124 units were corrected in a preprocessing step. This clock drift was inferred by comparing the RS
125 waveforms for five teleseismic events spanning the 10-day monitoring period with the ones
126 from the local BB seismic station where the internal clock is regularly synchronized via its
127 GPS receiver. Although this linear clock drift allows correlation with the BB waveforms, slight
128 deviations in linearity hamper the use of the three RS to reliably locate the local icequakes. To
129 power each of the RS3D units off-grid, a 100 Ah, 12 V leisure battery was used. The battery
130 voltage was dropped to 5 V for the Raspberry-Pi using a micro-USB DC 12–5 V power

131 inverter. RS power consumption, measured using an inline power consumption logger prior to
132 deployment, was estimated to be 2.8 W during start-up and 1.25 W during runtime. Additional
133 details about some of the more technical aspects of the RS can be found within the links and
134 code presented in Data and Resources.

135

136 In Antarctica, the preprogrammed RS sensors were set up in a north-facing triangular array at
137 the center of the BIA (Fig. 1). Because this is a pilot study, all sensors were placed near each
138 other (i.e., 90 m apart), with the intention of cross validating the recorded data set (with the
139 drawback of limiting the aperture and reducing the capability of locating distant seismic
140 events). The location of each site was marked with a flag to help relocate the RS units—though
141 the ice surface is slow-flowing and does not present any major hazard. The RS units were
142 weather sealed in a baseless wooden box screwed into the ice (Fig. 1c). Screws at each corner
143 of the RS enclosure enabled the RS to be leveled directly on the ice (although the screws
144 themselves did not penetrate the ice surface). The battery was wrapped in insulating foam to
145 preserve battery life and placed next to each RS. The RS units were powered simultaneously
146 by unique operators, who then sealed the protective box by screwing down a wooden lid.
147 Following installation, the site was left alone and not accessed again until the site had to be
148 decommissioned prior to the winter retreat of scientists from the summer-only research station.
149 No airplanes took off or landed on the local blue ice airfield (where the AWS is located; Fig.
150 1) during the monitoring period.

151

152 *Temperature measurements*

153 We compare our seismic data sets to temperature measurements to explore the link between
154 local temperature changes and BIA seismicity. We use hourly records from a local AWS to
155 examine diurnal fluctuations in air temperature (which is a major control of ice surface

156 temperature), and brightness data (collected by sensors onboard the Landsat 8 satellite) to
157 explore the regional variations in ice surface temperature that might drive spatial changes in
158 near-surface seismicity.

159

160 The closest AWS to our study site is located at the edge of the PEA airfield (Fig. 1), ~3 km
161 east of our RS network. The AWS was custom built for PEA by Konrad Steffen (Swiss Federal
162 Institute for Forest, Snow and Landscape Research, Boulder, Colorado), and it was installed in
163 the austral summer field season commencing in October 2012. It locally stores hourly air
164 temperature, humidity, pressure, wind speed, and wind direction on a Campbell data logger. In
165 this article, we report the average hourly temperature data collected by the Vaisala HMP45
166 temperature sensor (which was powered locally by solar energy) to explore the relationship
167 between air temperature and BIA seismicity. There are no data gaps during our survey period.

168

169 To retrieve surface temperature data across the area, we use collection 1, level 1 (terrain
170 corrected) imagery from the operational land imager (OLI) and the thermal infraRed sensor
171 (TIRS) onboard Landsat 8. OLI is a push broom imager with nine spectral bands (B1-9), which
172 record in the visible to near infrared spectrum, with a spatial resolution of 30 m or less (U.S.
173 Geological Survey [USGS]). In our study, we use OLI data for quality control purposes—to
174 improve TIRS resolution and pinpoint survey days where cloud cover is at a minimum. The
175 TIRS is a two-band push broom imager (B10–11), which records data at 100 m spatial
176 resolution (USGS). We use the TIRS B10 (centered on 10.9 μm) to extract at sensor brightness,
177 which is resampled to 30 m using the OLI. More details on this data set and our processing
178 methodology can be found in Data and Resources. We use data collected on 29 January 2020
179 at 07:01 local time (during our survey period), when cloud cover across the tile was at a
180 minimum(~8.2%) and local AWS measurements report a gradual rise in hourly air

181 temperature, as solar radiation increases from the night minimum, toward a mid-day maximum.
182 This data set allows us to examine regional variations in surface temperature that could drive
183 spatial variations in ice surface expansion and contraction.

184

185 **Results and Discussion**

186 Seismic signals were recorded by each of the RS units and the BB station during the 10-day
187 monitoring period (21–31 January 2020). Although measurements are consistently recorded in
188 RS2, RS3, and the BB station, four large data gaps in RS1 (amounting to 40% data loss over
189 the study period) suggest intermittent battery connectivity issues. As this data loss, together
190 with the clock issue (see the Methods section), restricts our ability to triangulate RS signals
191 and locate local seismic events, we only present data collected by RS2 (closest to PEA, the
192 AWS, and the BB station, Fig. 1). Because we document the first RS deployment in Antarctica,
193 we begin our Results and Discussion section by exploring seismic signal analysis and
194 conducting seismic instrument comparisons—to examine the data set collected by RS2. We
195 then summarize the advantages and limitations of the RS, to assist researchers planning to use
196 the RS in similar environments. The Blue ice seismicity section focuses on the scientific
197 findings of our study and the potential drivers of seismicity at our research site.

198

199 ***Background seismic noise level***

200 Level of background seismic noise is often used as an indicator of the quality of both site and
201 sensor installation and should accompany seismic recordings as an indication of the
202 completeness of the event catalog. To assess and compare background seismic noise level, the
203 median power spectral density (PSD) and median root mean square (rms) amplitude of
204 acceleration were computed for both RS2 and the BB station ELIS (Fig. 2). A 10-day period is
205 relatively short for monitoring the background noise, but our computation may provide a

206 preliminary trend in the PSD. Figure 2a reveals that the noise level of RS2 is consistently higher
207 than the one from the BB station (up to 30 dB at 10 Hz and at 10 s), which is an expected
208 observation considering the sensor types and the format of installation and insulation (Anthony
209 et al., 2019). Regarding RS2 PSD, at high frequency there is no significant difference in noise
210 level between daytime and nighttime (Fig. 2a). We also computed the PSD for a short 6 hr long
211 period of moderate wind (i.e., wind speed ~ 4.5 m/s). As expected, wind produces an increased
212 noise level on both vertical and horizontal components (with the RS protection box being an
213 obstacle to wind flow). During the 10-day monitoring period the median wind speed was low,
214 that is, 2.7 m/s. Favorably, the particular site of PEA, protected by the high mountains to the
215 south and southeast, is not affected by strong winds throughout the year (median wind speed
216 ~ 3.3 m/s). In the microseism period band, although the higher noise level in the RS2 entirely
217 masks the primary microseism ($T = 16$ s), the peak associated with the secondary microseism
218 ($T = 5\text{--}6$ s) is visible—but it cannot be clearly distinguished due to long-period RS self-noise
219 (Fig. 2a). At long period (when $T > 20$ s), our observed PSDs unequivocally approaches the
220 RS self-noise (Fig. 2a). We are therefore reluctant to interpret the small (about 5 dB) difference
221 between day and night PSDs. For the ELIS BB station, which has a lower seismic noise level
222 overall, there is a much larger difference between seismic noise recorded over the day and night
223 (~ 10 dB) at high frequency ($f > 2.5$ Hz) (Fig. 2a). We explore this relationship further in Figure
224 2b, which shows the average rms acceleration for the 10-day period, as a function of hour of
225 day for high frequency, that is, 5–20 Hz. Although the high-noise level in the RS2 is confirmed
226 for the entire day, the BB data are clearly dominated by anthropic noise between 07:00 and
227 19:00. This is a result of construction work, machinery, and staff movement at PEA throughout
228 the day, as the BB sensor is only 350 m from the main PEA building (Fig. 1). The PSD shows
229 that the wind effect is much less pronounced on the BB station though, as the sensor is protected
230 by a large metallic shelter. We also note that the noise level increases at long period ($T > 50$ s),

231 most probably as a result of atmospheric pressure change (Sorrells, 1971; De Angelis and
232 Bodin, 2012).

233

234 *Seismic signals*

235 During our 10-day survey period, the RS2 recorded 2936 short duration, high-frequency events
236 with relatively small ground velocity. Data (presented in Fig. 3) were initially filtered with a
237 band-pass filter between 5 and 20 Hz, whereas three template events were selected manually
238 to cross correlate the entire data set (after tries with three other unsuccessful patterns). The
239 extracted events have at least a 0.9 correlation coefficient with the template. Cross-correlation
240 plots in Figure 3a,b highlight the inherent high degree of similarity between seismic events,
241 whereas Figure 3c,d helps to showcase the detail of a typical event. These seismic signals are
242 characteristic of surface icequakes (Neave and Savage, 1970; Mikesell et al., 2012), derived
243 from a local source of small but frequent ice cracking. The frequency of short-duration seismic
244 signals, the dominance of surface waves, and the high degree of similarity among events
245 (combined with site specific measurements of ice flow, wind, and longer-term monitoring
246 of the area with the BB seismometer) rule out other mechanisms of seismicity in glaciated
247 environments (largely documented in cryoseismology reviews by Podolskiy and Walter, 2016,
248 and Aster and Winberry, 2017), such as stick-slip motion at the interface between the ice and
249 bed (e.g., Barcheck et al., 2018, and references therein), hydrofracturing as a result of lake
250 drainage (Carmichael et al., 2012), or teleseismic earthquake induced microseismicity (Peng et
251 al., 2014).

252

253 For comparison, we extracted seismic signals from the BB data set over time windows
254 encompassing the arrival times of icequakes detected on RS2 (Fig. 4). Seismic signals were
255 aligned on the largest amplitude found within a 1 s long window, moving from -5 to $+5$ s,

256 relative to the arrival time observed on RS2. The produced stack trace exhibits a high degree
257 of similarity with the data set (from the same BB seismometer) of January 2013 (Lombardi et
258 al., 2019). Furthermore, the distribution of these events (based on their time delay) shows a
259 clear discrimination within the data set (Fig. 5a). On one hand, there is a background signal of
260 about 50 events per 0.25 s bin distributed prior to and after the “0” reference lag, suggesting
261 that the BB station recorded numerous events in which surface-wave signals are in some way
262 coherent. Indeed, because of its low background noise (Fig. 2b), the BB station is able to record
263 many icequakes of smaller amplitude. On the other hand, though, two groups of events,
264 representing a total of 510, with delay time around ~ 1.0 and ~ 2.5 s, clearly emerge from the
265 background (referred as Group1s and Group2.5s, hereafter) - which could therefore be
266 associated with the signal detected by RS2. The substacks computed for these two groups of
267 events are characterized by amplitude differences. Although the most populated substack of
268 Group2.5s (pink line in Fig. 5) exhibits the smallest amplitude on the BB station and the largest
269 amplitude on RS2, the substack of Group1s (blue line in Fig. 5) exhibits exactly the opposite
270 trend. Group1s best matches the January 2013 waveform (dashed line in Fig. 5d) recorded by
271 Lombardi et al. (2019). Considering these amplitude observations and the values of time delay,
272 we may postulate that Group2.5s, with a time delay of ~ 2.5 s, can be explained by a
273 propagation of surface waves from the RS2 blue ice to the BB station. Considering the distance
274 between the two sites (i.e., 4.5 km), this represents a propagation velocity of about 1.8 km/s,
275 which is a reasonable estimate (even considering the timing synchronization uncertainties) for
276 surface-wave propagation within the ice and firm (Mikesell et al., 2012; Diez et al., 2016). The
277 second group of seismic signals (Group1s), which exhibits the smallest amplitude on RS2 and
278 the largest amplitude on the BB data set, has an associated short-time delay of ~ 1.0 s. This
279 would favor a seismogenic source closer to the BB station and further away from RS2. A
280 possible candidate may be the tip of the elongated BIA on Utsteinen Nunatak leeward-side

281 (visible in Fig. 1), which is some 1.5 km east of RS2. However, for such a distance, one may
282 expect a seismic signal of longer duration, with less high-frequency content than the ones
283 observed for Group2.5s. In absence of bedrock geometry and any seismic velocity model, this
284 discussion remains only speculative at this stage of the study. A seismic network with more
285 stations covering a much wider area (i.e., hundreds rather than tens of meters) together with ice
286 penetrating radar investigations of the subsurface might help to unravel these peculiar icequake
287 observations.

288

289 *Raspberry Shake performance*

290 Our RS2 unit recorded 2936 icequakes at our study site in Antarctica over a 10-day monitoring
291 period. These findings illustrate that RS units can record specific, localized phenomenon (such
292 as icequakes) in extreme environments (which are often detectable within the noise
293 environment only at local distances) and that these measurements can be used to complement
294 more wide-ranging and longer-term BB seismometer measurements (where these are
295 available). Other authors have also tested RS performance, however, in less extreme
296 environments (e.g., Manconi et al., 2018). These authors found the RS to be a viable solution
297 for monitoring rockfall in the Swiss Alps, where they gathered more than 1 yr of data with
298 relatively low noise levels, allowing the detection of several rockfall events, aided by visual
299 imagery. They remark, however, that care should be made when using RS to monitor processes
300 that are characterized by long-period signals (>10 s), as RS units are 4.5 Hz geophone sensors.
301 Unfortunately, there is limited literature focusing on RS research applications, so we cannot
302 state the potential use of the RS for other research scopes at this stage. In the following
303 paragraphs, we highlight the positive attributes of the RS for our research project, and the
304 limitations of our survey. We then summarize recommendations for future RS deployments in
305 similar glaciated environments.

306

307 Our survey shows that the RS is a good short-period sensor, which performs well in cold
308 environments such as Antarctica (though our monitoring period was relatively short and
309 conducted during the austral summer). There is no evidence of function loss in the cold (air
310 temperatures reached -15.0°C during our survey period) or during periods of rapid temperature
311 change. For our remote study, where internet access was not available, site installation was
312 simplified with preprogramming of the RS units, with the date and time of installation being
313 set after power-up. After the survey period, we downloaded data over ethernet from the RS.
314 For a limited number of sensors, this is a straightforward procedure. For a large number of
315 sensors, a nodal solution may be easier to handle.

316

317 For our survey there were some limitations. We note that RS1 experienced intermittent battery
318 connectivity issues, which restricted data triangulation with RS2 and RS3. Icequakes, detected
319 in all three RS devices are clearly discernible in the seismic record, but relatively high self-
320 noise may mask some other seismic signals from more distant source locations. Although the
321 RS units can be deployed without internet connectivity and GPS antenna (as ours were), during
322 our survey we recorded an internal clock-drift that substantially restricted our ability to locate
323 icequake sources and take full advantage of the three-component data set. Although this clock-
324 drift was subsequently partly corrected with the GPS-enabled BB station, we note that a longer
325 term study is likely to have more significant timing issues, if deployed in the same way.

326

327 Our recommendations for improvements in future deployments of the RS in similar
328 environments are based on the survey limitations we note in the previous paragraph. Battery
329 connectivity issues may be resolved using newer batteries, and newer battery connections (we
330 used older batteries and connections due to the time constraints associated with battery

331 shipment to Antarctica). Beyond a relatively high-RS self-noise level, seismic background
332 noise may be reduced if the RS units were better protected from the elements, specifically
333 blowing snow and high winds (though at PEA average wind speed is moderate) and the large
334 daily variations in air temperature (associated with solar radiation). We suggest that RS sensors,
335 placed in insulated, protective cases, should be installed 20–30 cm or more below the surface,
336 with adapted sensor feet screwed into the ice for a better ground coupling. Timing issues will
337 improve significantly with Internet access. However, if Internet access is unavailable (as it is
338 in many extreme environments) timing could be provided with the implementation of an
339 external GPS antenna, which will connect to the RS unit via USB and/or the Raspberry-Pi
340 general-purpose input/output pins. This has power draw implications of ~40 mA (Raspberry
341 Shake, personal comm., 2021), which can be handled with an increase of the power supply
342 capacity.

343

344 ***Blue ice seismicity***

345 Figure 6 contains a plot of all known icequakes detected by RS2 and their relationship to local
346 air temperature measurements (recorded by the nearby AWS, Fig. 1). This graph shows a
347 remarkable periodicity in the occurrence of icequakes. Events are recorded daily across the
348 monitoring period, appearing as swarms at very similar times of the day, with consistent
349 interevent spacing (of 60 s on average). These cyclic seismic recordings match changes in air
350 temperature. All seismic events occur during times of minimum air temperature, as
351 temperatures drop during the night period, between approximately 18:00 and 03:00 local time.
352 The timing of icequakes and their relationship with air temperature changes indicate a clear
353 diurnal modulation of seismicity; suggesting that icequakes are generated by the thermal
354 contraction of the blue ice surface as it cools (Butkovich, 1959).

355

356 To explore the role ice surface temperatures play in blue ice seismicity, we use data collected
357 by sensors onboard Landsat 8. Figure 7 shows that during an orbital pass on 29 January at
358 07:01 local time, the wind-scoured BIA (where RS2 was installed) had a surface temperature
359 of -9°C to -10°C , which is $\sim 3^{\circ}\text{C}$ warmer than surrounding snow-covered ice (which was
360 -12°C or colder). Although this recording was taken at one of the colder times of the day (and
361 orbital revisit frequency prevents more detailed analysis of diurnal changes in surface
362 temperature), these measurements suggest that BIAs have different thermal regimes to
363 surrounding ice flows. We attribute these differences to regional variations in surface albedo
364 and katabatic wind flow (Takahashi et al., 1992; Bøggild et al., 1995; Bintanja, 2000). As BIAs
365 typically have an albedo of ~ 0.6 and fresh snow usually has an albedo > 0.78 (Winther et al.,
366 1996; Reijmer et al., 2001), BIAs are likely to experience greater temperature fluctuations on
367 diurnal cycles, as a result of differential solar gain. The regional differences in surface
368 temperatures in Figure 7 therefore demonstrate that BIAs, such as the one we examine at our
369 study site, are likely to experience greater thermal expansion and contraction than neighboring
370 snow-covered ice. These temperature measurements help to explain why icequakes are so
371 numerous at our study site.

372

373 **Conclusions**

374 An RS seismic sensor installed on the blue ice surface close to the PEA research station
375 detected 2936 icequakes over a 10-day monitoring period in January 2020. About 1/6 of them
376 can be linked to seismic events recorded by the local BB station and can be associated with
377 icequake seismicity revealed in a previous study. Therefore, our seismic signal analysis reveals
378 that the RS is capable of monitoring specific localized phenomenon (such as icequakes) in cold,
379 glaciated environments. Outputs like these can be used as a precursor for further study or to
380 complement data collected by permanent BB stations, which record wider-scale and longer

381 term seismicity, with low background noise (but with the cost of more sophisticated installation
382 and maintenance).

383

384 Our investigations of blue ice seismicity reveal that the timing and frequency of icequakes are
385 related to diurnal fluctuations in air temperature and regional variations in surface temperature,
386 linked to solar gain, katabatic wind flow regimes, and surface albedo. As ice surface
387 temperatures change, Antarctic BIAs undergo thermal expansion and contraction, generating
388 thousands of high-frequency icequakes. Although these icequakes are too small to be a threat
389 to ice sheet stability, icequake recordings such as ours can be used to monitor the thermal state
390 and ice fracture mechanics of ablation zones in Antarctica, which are difficult to monitor by
391 other means.

392

393 **Data and Resources**

394 Seismic data presented in this article are freely available to download from online data
395 repositories. Our Raspberry Shake (RS) seismic measurements are accessible through RS
396 International Federation of Digital Seismograph Networks (FDSN) web services available at
397 <https://raspberrysake.org/data-center/> (last accessed February 2021) (doi:10.7914/SN/AM),
398 and technical specifications of the RS seismic sensors can be accessed at
399 <https://manual.raspberrysake.org/specifications.html#techspecs> (last accessed February
400 2021). Broadband (BB) seismic data from the ELIS BB station at the Princess Elisabeth
401 Antarctica (PEA) research station will soon be available from the Orfeus Data Center (ODC)
402 web services (fdsn dataselect) and, in the meantime, are available upon request to the Royal
403 Observatory of Belgium (ROB)—Seismology-Gravimetry section (seismo.info@oma.be).
404 Both seismic data sets were processed using standard processing steps, taking advantage of the
405 Geophysical Investigations in Seismology using MATLAB Objects (GISMO) toolbox for

406 MATLAB (www.mathworks.com/products/matlab, last accessed February 2021), and the
407 ObsPy package for Python. Surface temperature measurements from Landsat 8 are freely
408 available to download from <https://earthexplorer.usgs.gov> (last accessed January 2021). We
409 use the ACOLITE Landsat 8 processor available at
410 <https://odnature.naturalsciences.be/remsem/software-and-data/acolite> (last accessed January
411 2021) to extract at-sensor brightness data from Landsat 8 available at
412 <https://earthexplorer.usgs.gov/> (last accessed January 2021).

413

414 **Acknowledgements**

415 Antarctic fieldwork was funded by the Baillet Latour Antarctica Fellowship, awarded to Kate
416 Winter in October 2018. The three RS3D sensors were purchased through Northumbria
417 University's Extreme Environments research grant. Staff from the International Polar
418 Foundation at the Princess Elisabeth Antarctica (PEA) research station are thanked for their
419 assistance with the research project and their help to maintain the broadband (BB) seismic
420 station—ELIS. The authors are grateful for the air temperature data provided to them by
421 Konrad Steffen at the Swiss Federal Institute for Forest, Snow and Landscape Research.
422 Konrad Steffen strove to collect meteorological data in the most remote places on Earth during
423 his esteemed research career. The glaciology community acknowledges him for his
424 considerable contribution to Science in polar and alpine regions. The authors thank Thierry
425 Camelbeeck and Thomas Lecocq (Royal Observatory of Belgium [ROB]) for access to the BB
426 seismic data (who in turn acknowledge the financial support of ELIS through Belgian Science
427 Policy Contracts EA/33/2A and EA/33/2B), Maxime Bès de Berc (Institut de physique du
428 globe de Strasbourg [IPGS]) and Robert Anthony (U.S. Geological Survey [USGS]) for the
429 Raspberry Shake (RS) self-noise information, and the RS team for their assistance and
430 encouragement. The authors are grateful for the constant development of the following

431 software packages used in this study: GISMO Seismic Analysis Toolbox (Reyes and West,
432 2011; Thompson and Reyes, 2018), Matplotlib (Hunter, 2007), Python (python.org), and
433 ObsPy (Beyreuther et al., 2010), and the authors thank the National Aeronautics and Space
434 Administration [NASA]/USGS for the acquisition and free distribution of Landsat 8 images
435 and Quinten Vanhellemont (RBINS) for assistance with ACOLITE. The authors also wish to
436 extend gratitude to Myrto Pirlı (Guest Editor) and two anonymous reviewers for their insightful
437 and constructive comments.

438

439 **References**

- 440 Anthony, R.E., A. T. Ringler, D. C. Wilson, and E. Wolin (2019). Do Low-Cost
441 Seismographs Perform Well Enough for Your Network? An Overview of Laboratory
442 Tests and Field Observations of the OSOP Raspberry Shake 4D, *Seismol. Res. Lett.*
443 *90*(1) 219-228.
- 444 Aster, R. C., and J. P. Winberry (2017). Glacial seismology, *Rep. Prog. Phys.* **80**(12)
445 126801.
- 446 Barcheck, C. G., S. Tulaczyk, S. Y. Schwartz, J. I. Walter, and J. P. Winberry (2018).
447 Implications of basal micro-earthquakes and tremor for ice stream mechanics: Stick-
448 slip basal sliding and till erosion, *Earth and Planet. Sci. Lett.* **486** 54-60.
- 449 Bès de Berc, M., R. Pestourie, H. Jund, and C. Broucke (2019). A complete characterization
450 of 27 OSOP Raspberryshakes performed at EOST Seismic Instrumentation Facility,
451 *Geophys. Res. Abstr.* **21**, EGU2019-16607.
- 452 Beyreuther, M., R. Barsch, L. Krischer, T. Megies, Y. Behr, and J. Wassermann (2010).
453 Obspy: a python toolbox for seismology, *Seismol. Res. Lett.* **81**(3) 530–533.
- 454 Bintanja, R., and M. R. van den Broeke (1995). The surface energy balance of Antarctic
455 snow and blue ice, *J. Appl. Meteorol.* **34**(4) 902–926.
- 456 Bintanja, R. (1999). On the glaciological, meteorological, and climatological significance of
457 Antarctic blue ice areas, *Rev. Geophys.* **37**(3) 337–359.
- 458 Bintanja, R. (2000). Surface heat budget of Antarctic snow and blue ice: interpretation of
459 spatial and temporal variability, *J. Geophys. Res.: Atmos.* **105**(D19) 24387–24407.
- 460 Bøggild, C. E., J.-G. Winther, K. Sand, and H. Elvehøy (1995). Sub-surface melting in blue

461 ice fields in Dronning Maud Land, Antarctica: observations and modelling, *Ann.*
462 *Glaciol.* **21**162–168.

463 Butkovich, T. (1959). Thermal expansion of ice, *J. Appl. Phys.* **30** 350.

464 Calais E, D. Boisson, S. Symithe, C. Prépetit, B. Pierre, S. Ulyse, L. Hurbon, A. Gilles, J.-M.
465 Théodat, T. Monfret, A. Deschamps, F. Courboulex, J. Chèze, F. Peix, E. Bertrand, J.-
466 P. Ampuero, B. Mercier de Lépinay, J. Balestra, J.-L. Berenguer, R. Bossu, L. Fallou,
467 and V. Clouard (2020). A Socio-Seismology experiment in Haiti, *Front. Earth Sci.*
468 **8**:542654.

469 Carmichael, J. D., E. C. Pettit, M. Hoffman, A. Fountain, and B. Hallet, B. (2012). Seismic
470 multiplet response triggered by melt at Blood Falls, Taylor Glacier, Antarctica, *J.*
471 *Geophys. Res.: Earth Surf.* **117**(F3).

472 Cochran, E. S. (2018). To catch a quake, *Nat. Commun.* **9** 2508.

473 De Angelis, S., and P. Bodin, (2012). Watching the Wind: Seismic Data Contamination at
474 Long Periods due to Atmospheric Pressure-Field-Induced Tilting. *Bull.*
475 *Seismol. Soc. America* **102**(3), 1255–1265.

476 Diaz, J., M. Schimmel, M. Ruiz, and R. Carbonell (2020). Seismometers within cities: a tool
477 to connect Earth Sciences and Society, *Front. Earth Sci.* **8** (9) 1-7.

478 Diez, A., P. D. Bromirski, P. Gerstoft, R. A. Stephen, R. E. Anthony, R. C. Aster, C. Cai, A.
479 Nyblade, and D. A. Wiens (2016). Ice shelf structure derived from dispersion curve
480 analysis of ambient seismic noise, Ross Ice Shelf, Antarctica, *Geophys. J. Int.* **205** (2)
481 785-795.

482 Hunter, J.D. (2007). Matplotlib: a 2D graphics environment. *Comput. Sci. Eng.* **9** 90–95.

483 Jeddi, Z., P. H. Voss, M.B. Sørensen, F. Danielsen, T. Dahl-Jensen, T. B. Larsen, G. Nielsen,
484 A. Hansen, P. Jakobsen, and P. O. Frederiksen (2020). Citizen Seismology in the
485 Arctic, *Front. Earth Sci.* **8** (139).

486 Lecocq, T. and 76 others (2020). Global quieting of high-frequency seismic noise due to
487 COVID-19 pandemic lockdown measures, *Science* **369**(6509) 1338–1343.

488 Lombardi, D., I. Gorodetskaya, G. Barruol, and T. Camelbeeck (2019). Thermally induced
489 icequakes detected on blue ice areas of the East Antarctic ice sheet, *Ann. Glaciol.* **60**
490 (79) 45-56.

491 MacAyeal, D., A. Banwell, E. Okal, J. Lin, L. Willis, B. Goodsell, and G. MacDonald
492 (2019). Diurnal seismicity cycle linked to subsurface melting on an ice shelf, *Ann.*
493 *Glaciol.* **60**(79) 137-157.

494 Manconi, A., V. Cobiello, M. Galletti, and R. Seifert (2018). Monitoring rockfalls with
495 the Raspberry Shake, *Earth Surf. Dynam.* **6**(4) 1219-1227.

496 McNamara, D. E. and R. P. Bulland (2004). Ambient Noise Levels in the Continental United
497 States, *Bull. Seismol. Soc. Am.* **94**(4) 1517–1527.

498 Mikesell, T. D., K. Van Wijk, M. M. Haney, J.H. Bradford, H. P. Marshall, and J. T. Harper
499 (2012). Monitoring glacier surface seismicity in time and space using Rayleigh
500 waves, *J. Geophys. Res.: Earth Surf.* **117** F02020.

501 Mouginit, J., E. Rignot, and B. Scheuchl (2019). Continent-wide, interferometric SAR
502 phase, mapping of Antarctic ice velocity, *Geophys. Res. Lett.* **46** 9710–9718.

503 Neave, K., and J. Savage (1970). Icequakes on the Athabasca glacier, *J. Geophys. Res.* **75**(8)
504 1351–1362.

505 Nishio, F (1983). Studies on thermally induced fractures and snowquakes of polar snow
506 cover, *Memoirs of National Institute of Polar Res. Ser. C.* **14** 1–48.

507 Olinger, S. D., B. P. Lipovsky, D. A. Wiens, R. C. Aster, P. D. Bromirski, Z. Chen, P.
508 Gerstoft, A. A. Nyblade, and R. A. Stephen (2019). Tidal and Thermal Stresses Drive
509 Seismicity Along a Major Ross Ice Shelf Rift, *Geophys. Res. Lett.* **46** (12) 6644–
510 6652.

511 Pattyn, F, K. Matsuoka, and J. Berte (2010). Glacio-meteorological conditions in the vicinity
512 of the Belgian Princess Elisabeth Station, Antarctica, *Antarct. Sci.* **22**(1) 79–85.

513 Peng, Z., J. I., Walter, R. C. Aster, A. Nyblade, D. A. Wiens, and S. Anandkrishnan (2014).
514 Antarctic icequakes triggered by the 2010 Maule earthquake in Chile. *Nat. Geo.* **7**(9)
515 677-681.

516 Peterson, J. (1993). Observations and Modeling of Seismic Background Noise, *USGS Open-*
517 *File Report 93-322*, U. S. Geological Survey, Albuquerque, New Mexico.

518 Podolskiy, E. A., and F. Walter (2016). Cryoseismology, *Rev. Geophys.*, **54**(4) 708–758.

519 Podolskiy, E.A., K. Fujita, S. Sunako, A. Tsushima, and R. B. Kayastha (2018). Nocturnal
520 thermal fracturing of a Himalayan debris covered glacier revealed by ambient
521 seismic noise, *Geophys. Res. Lett.* **45**(18) 9699–9709.

522 Reijmer C., R. Bintanja, and W. Greuell (2001). Surface albedo measurements over snow and
523 blue ice in thematic mapper bands 2 and 4 in Dronning Maud Land, Antarctica, *J.*
524 *Geophys. Res.: Atmos.* **106**(D9) 9661–9672.

525 Reyes, C. G., and M. E. West (2011). The waveform suite: A robust platform for
526 manipulating waveforms in MATLAB, *Seis. Res. Lett.* **82**(1) 104–110.

527 Sleeman, R., van Wettum, A. and J. Trampert (2006). Three-Channel Correlation Analysis:

528 A New Technique to Measure Instrumental Noise of Digitizers and Seismic Sensors,
529 *Bull. Seismol. Soc. America* **96**(1) 258–271.

530 Sorrells, G. G. (1971). A preliminary investigation into the relationship between long-period
531 seismic noise and local fluctuations in the atmospheric pressure field, *Geophys. J.*
532 *International* **26**(1-4) 71–82.

533 Subedi, S., G. Hetényi, P. Denton, and A. Sauron (2020). Seismology at School in Nepal: A
534 Program for Educational and Citizen Seismology Through a Low-Cost Seismic
535 Network, *Front. Earth Sci.* **8** (73).

536 Takahashi, S., T. Endoh, N. Azuma, and S. Meshida (1992). Bare ice fields developed in
537 the inland part of Antarctica, *Proc. NIPR Symp. Polar Meteorol. Glaciol.* **5** 128–139.

538 Taruselli, M., D. Arosio, L. Longoni, M. Papini, and L. Zanzi (2019). Raspberry Shake
539 Sensor Field Tests for Unstable Rock Monitoring, *Near Surface Geoscience*
540 *Conference and Exhibition: 8-12 September 2019, The Hague, Netherlands.*

541 Thompson G. and Reyes, C. (2018). GISMO - a seismic data analysis toolbox for MATLAB
542 (Version 1.20b) [software package]. Available at: [http://geoscience-](http://geoscience-communitycodes.github.io/GISMO/)
543 [communitycodes.github.io/GISMO/](http://geoscience-communitycodes.github.io/GISMO/). Accessed: Feb 11, 2020.
544 <http://doi.org/10.5281/zenodo.1404723>.

545 Welch, P. D. (1967). The use of fast Fourier transform for the estimation of power spectra: A
546 method based on time averaging over short, modified periodograms, *IEEE Trans.*
547 *Audio Electroacoust.* **15**(2) 70–73.

548 Winther, J.-G., H. Elvehøy, C. E. Bøggild, K. Sand, and G. Liston (1996). Melting, runoff
549 and the formation of frozen lakes in a mixed snow and blue-ice field in Dronning
550 Maud Land, Antarctica, *J. Glaciol.* **42**(141) 271–278.

551 Winther, J.-G., M. Jespersen, and G. Liston (2001). Blue-ice areas in Antarctica derived from
552 NOAA AVHRR satellite data, *J. Glaciol.* **47**(157) 325–334.

553 Zhang, T., Y. Chen, M. Ding, Z. Shen, Y. Yang, and Q. Guan (2019). Air-temperature
554 control on diurnal variations in microseismicity at Laohugou Glacier No. 12, Qilian
555 Mountains, *Annals of Glaciology* **60**(79) 125-136.

556

557 **List of Figure Captions**

558

559 **Figure 1.** Figure 1. Raspberry Shake (RS) installation site, on a 1.5-km-long blue ice area
560 (BIA) west of Princess Elisabeth Antarctica (PEA) research station. (a) Location map (from
561 Landsat 8 satellite imagery, acquired in January 2020) showing the main features of the study
562 site where we highlight the location of the three RS devices (brown squares), and in particular
563 RS2 on the BIA, as well as the PEA research station (red star), the automatic weather station
564 (AWS, green triangle), and the local broadband (BB) seismic station (yellow circle). (b) Map
565 shows the location of the field area on the East Antarctic Ice Sheet (EAIS). The West Antarctic
566 Ice Sheet (WAIS) is also annotated for reference. (c) Photograph of the RS setup: RS leveled
567 directly on the ice and connected to an insulated battery box through a power inverter. Note
568 that the wooden box (drilled into the ice) was used to provide protection from blowing snow.
569 (d) Field photograph showing RS2 (in wooden box) with a red flag to mark its location.

570

571 **Figure 2.** Comparisons between the RS2 sensor and the local ELIS BB station (a) power
572 spectral density (PSD) over the 10-day monitoring period for RS2 and the BB station. Thick
573 dashed lines show daytime at PEA research station (10:00–17:00) whereas thick solid lines
574 show “night” hours (22:00–05:00) when no one is working at the PEA research station. The
575 east component is shown for windy and calm conditions (thin dashed lines). The vertical
576 component for windy conditions is also shown (dotted lines). The presented RS self-noise data
577 are from Bès de Berc et al. (2019) and was calculated using the Sleeman method (Sleeman et
578 al., 2006). The observed higher level of the PSD, for EHE at $T > 0.7$ s, may reflect a higher
579 level of self-noise for the horizontal component (M. Bès de Berc, personal comm., 2021). “SM”
580 and “PM” stand for secondary and primary microseisms, respectively. New high- and low-
581 noise level models (NHNM and NLNM, respectively) represent the calculated noise models
582 from long duration records of worldwide seismic stations (Peterson, 1993). The PSD was
583 computed with ObsPy package (Beyreuther et al., 2010). The data set was processed using a
584 one-hour long segment overlapping by 50%, with 1/8 octave step and 1/4 of octave smoothing
585 (Welch, 1967; McNamara and Buland, 2004). The continuous data set in the frequency content
586 is shown in (b), which displays the median root mean square (rms) amplitude of acceleration
587 for the 10-day period as a function of the time of day for RS2 (black) and the BB station (gray).
588 Seismic traces were bandpassed between 5 and 20 Hz, and amplitudes were averaged over a
589 one-minute-long sliding window. Note that the BB data are clearly dominated by anthropic
590 noise between 07:00 and 19:00.

591

592 **Figure 3.** Icequakes recorded by RS2. (a) Cross-correlation plot of the 2936 icequake events
593 detected at RS2; (b) stack trace of all recorded icequakes and the average signal (black line);
594 (c) three component record of a typical icequake and (d) its frequency spectrum. Note that the
595 horizontal components (EHN and EHE) were not synchronized with the BB data, and therefore
596 their timing is unreliable.

597

598 **Figure 4.** Five hundred individual traces randomly chosen from the 2936 seismic traces from
599 (a) the BB data set and (b) the linear stack for the complete data set (solid line), with the
600 standard deviation noted (b, gray lines). The seismic signal was band-pass filtered between 5
601 and 20 Hz and aligned on the surface-wave largest peak (found by exploring ± 5 s around the
602 arrival time at RS2). The stack trace from events detected by the same BB seismometer in
603 January 2013 (Lombardi et al., 2019) is included for comparison (dashed line in b). This stack
604 trace was normalized to match the largest amplitude of the stack trace from this study. Note
605 that the P wave is not visible in the stack traces and the indicated timing is from Lombardi et
606 al. (2019).

607

608 **Figure 5.** Distribution of seismic signals on the BB data set, based on detection from RS2. (a)
609 Icequake distribution, presented in number of events, across the time delay—of the arrival time
610 of the largest amplitude of the signal (within ± 5 s after the arrival time detected on RS2 data
611 set). Note that the collected time delays are binned for every 0.25 s. Bins around 1 and 2.5 s
612 (gathering more than 80 events) were selected as the largest bins. Bins representing the average
613 number of events (around 50 events) are also shown for reference (bins -3.5 and +3.5 s). The
614 colored boxes on (a) show the time delay of stacked seismic signals from the BB data set,
615 displayed as a function of amplitude (meters per square second) in (d). (b) PSD of Group1s and
616 Group2.5s are displayed on top of median PSD calculated over the 10-day monitoring period
617 to show their importance relative to the background noise level. (c) Binned seismic signals on
618 RS2.

619

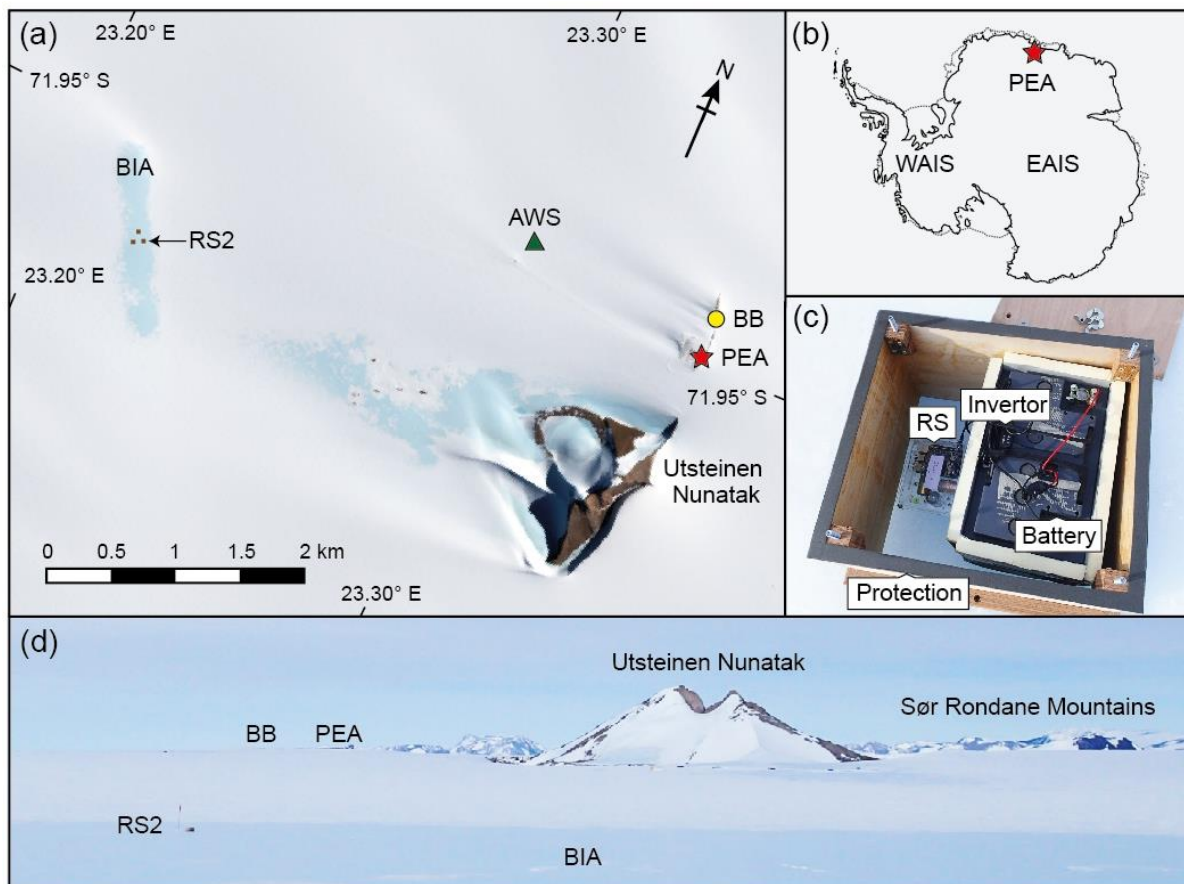
620 **Figure 6.** Time history of the recorded events (small orange dots) in RS2, with the interevent
621 spacing noted on the left y axis. Large orange circles with standard deviation bars show the
622 average interevent time whereas large green crosses show the total number of events per day,
623 corresponding to the right y axis in green. The small green crosses connected by green lines
624 show the number of events per hour. Average air temperature (light blue line) recorded by the

625 nearest AWS station is plotted on top. All events occur during times of minimum air
626 temperatures, during the night period, between approximately 18:00 and 03:00 local time.

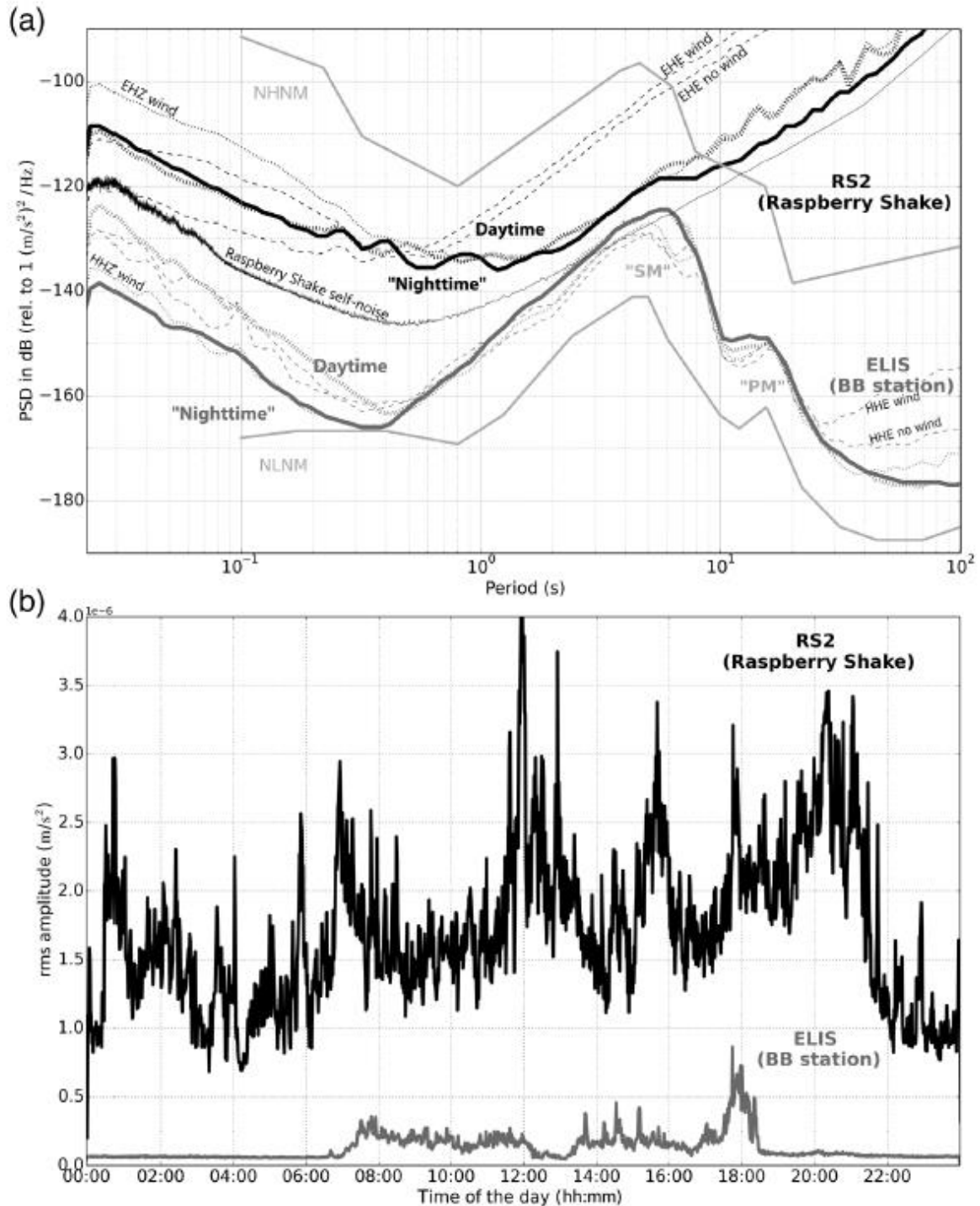
627

628 **Figure 7.** At sensor brightness measurements from the thermal infrared sensor (TIRS) onboard
629 Landsat 8, collected across the field site during an orbital pass on 29 January, at 07:01 local
630 time. The resultant surface temperature map (layered above a hillshade map) shows elevated
631 surface temperature measurements around Utsteinen nunatak (which is largely free of snow
632 and ice) and on wind-scoured surfaces west of the nunatak, including our study site, where BIA
633 surface temperatures are approximately 3°C warmer than surrounding snow-covered ice during
634 this early morning orbital pass. This suggests that BIAs could be more prone to larger
635 fluctuations in surface temperature (due to differences in albedo and thermal insulation),
636 generating increased surface expansion and contraction (as well as associated seismicity) in
637 BIAs, compared to neighboring ice flows.

638 **Figures**



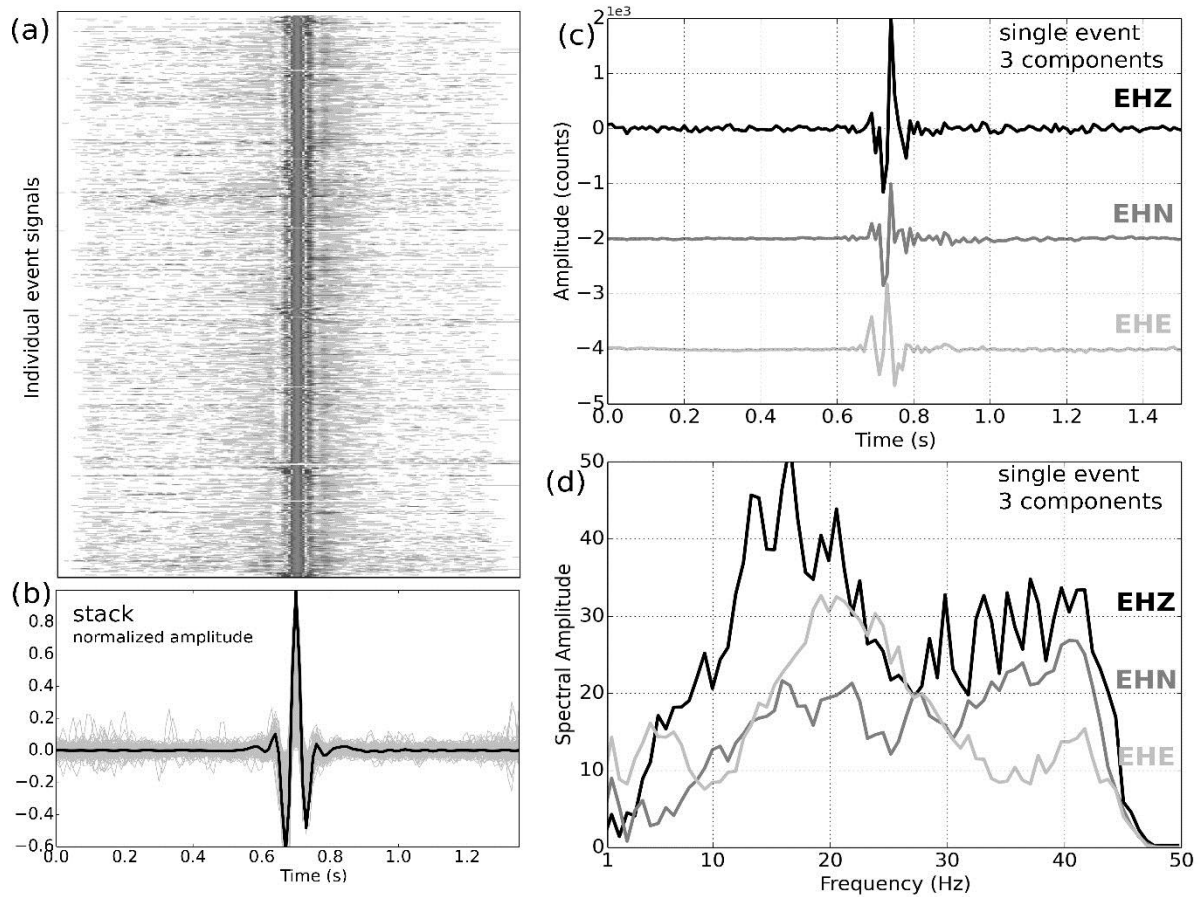
639
 640 **Figure 1.** Raspberry Shake (RS) installation site, on a 1.5-km-long blue ice area (BIA) west of
 641 Princess Elisabeth Antarctica (PEA) research station. (a) Location map (from Landsat 8
 642 satellite imagery, acquired in January 2020) showing the main features of the study site where
 643 we highlight the location of the three RS devices (brown squares), and in particular RS2 on the
 644 BIA, as well as the PEA research station (red star), the automatic weather station (AWS, green
 645 triangle), and the local broadband (BB) seismic station (yellow circle). (b) Map shows the
 646 location of the field area on the East Antarctic Ice Sheet (EAIS). The West Antarctic Ice Sheet
 647 (WAIS) is also annotated for reference. (c) Photograph of the RS setup: RS leveled directly on
 648 the ice and connected to an insulated battery box through a power invertor. Note that the
 649 wooden box (drilled into the ice) was used to provide protection from blowing snow. (d) Field
 650 photograph showing RS2 (in wooden box) with a red flag to mark its location.



651

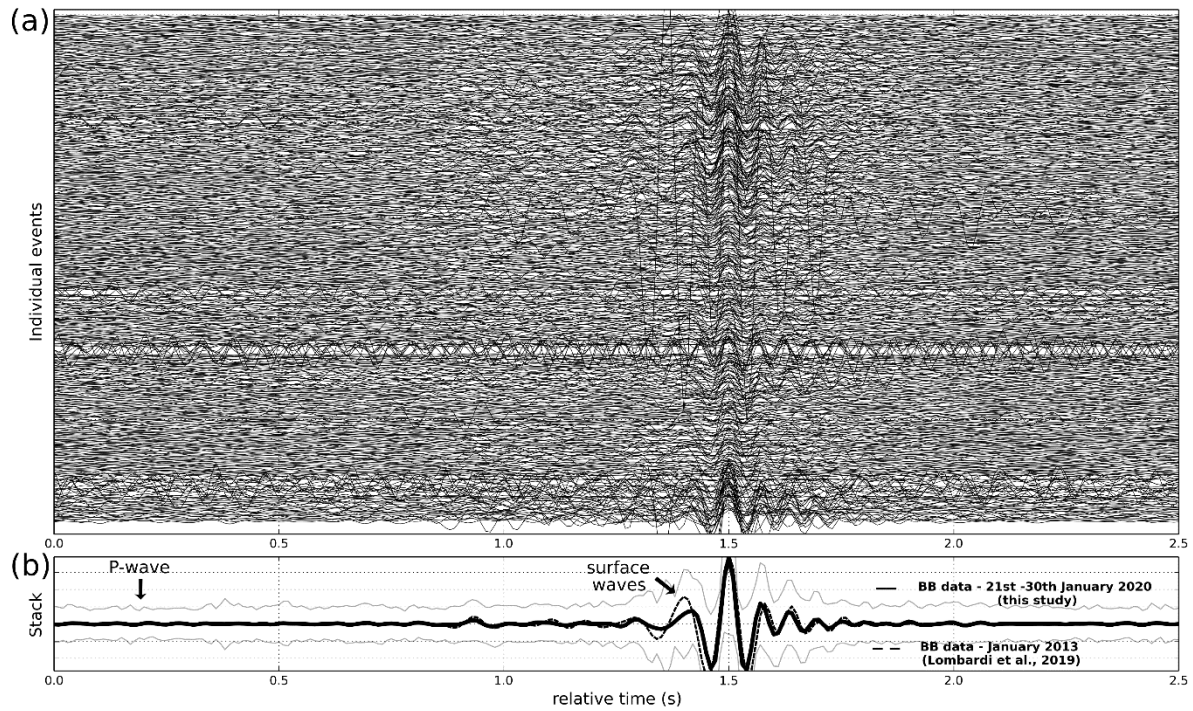
652 **Figure 2.** Comparisons between the RS2 sensor and the local ELIS BB station (a) power
 653 spectral density (PSD) over the 10-day monitoring period for RS2 and the BB station. Thick
 654 dashed lines show daytime at PEA research station (10:00–17:00) whereas thick solid lines
 655 show “night” hours (22:00–05:00) when no one is working at the PEA research station. The
 656 east component is shown for windy and calm conditions (thin dashed lines). The vertical
 657 component for windy conditions is also shown (dotted lines). The presented RS self-noise data
 658 are from Bès de Berc et al. (2019) and was calculated using the Sleeman method (Sleeman et

659 al., 2006). The observed higher level of the PSD, for EHE at $T > 0.7$ s, may reflect a higher
660 level of self-noise for the horizontal component (M. Bès de Berc, personal comm., 2021). “SM”
661 and “PM” stand for secondary and primary microseisms, respectively. New high- and low-
662 noise level models (NHNM and NLNM, respectively) represent the calculated noise models
663 from long duration records of worldwide seismic stations (Peterson, 1993). The PSD was
664 computed with ObsPy package (Beyreuther et al., 2010). The data set was processed using a
665 one-hour long segment overlapping by 50%, with 1/8 octave step and 1/4 of octave smoothing
666 (Welch, 1967; McNamara and Buland, 2004). The continuous data set in the frequency content
667 is shown in (b), which displays the median root mean square (rms) amplitude of acceleration
668 for the 10-day period as a function of the time of day for RS2 (black) and the BB station (gray).
669 Seismic traces were bandpassed between 5 and 20 Hz, and amplitudes were averaged over a
670 one-minute-long sliding window. Note that the BB data are clearly dominated by anthropic
671 noise between 07:00 and 19:00.



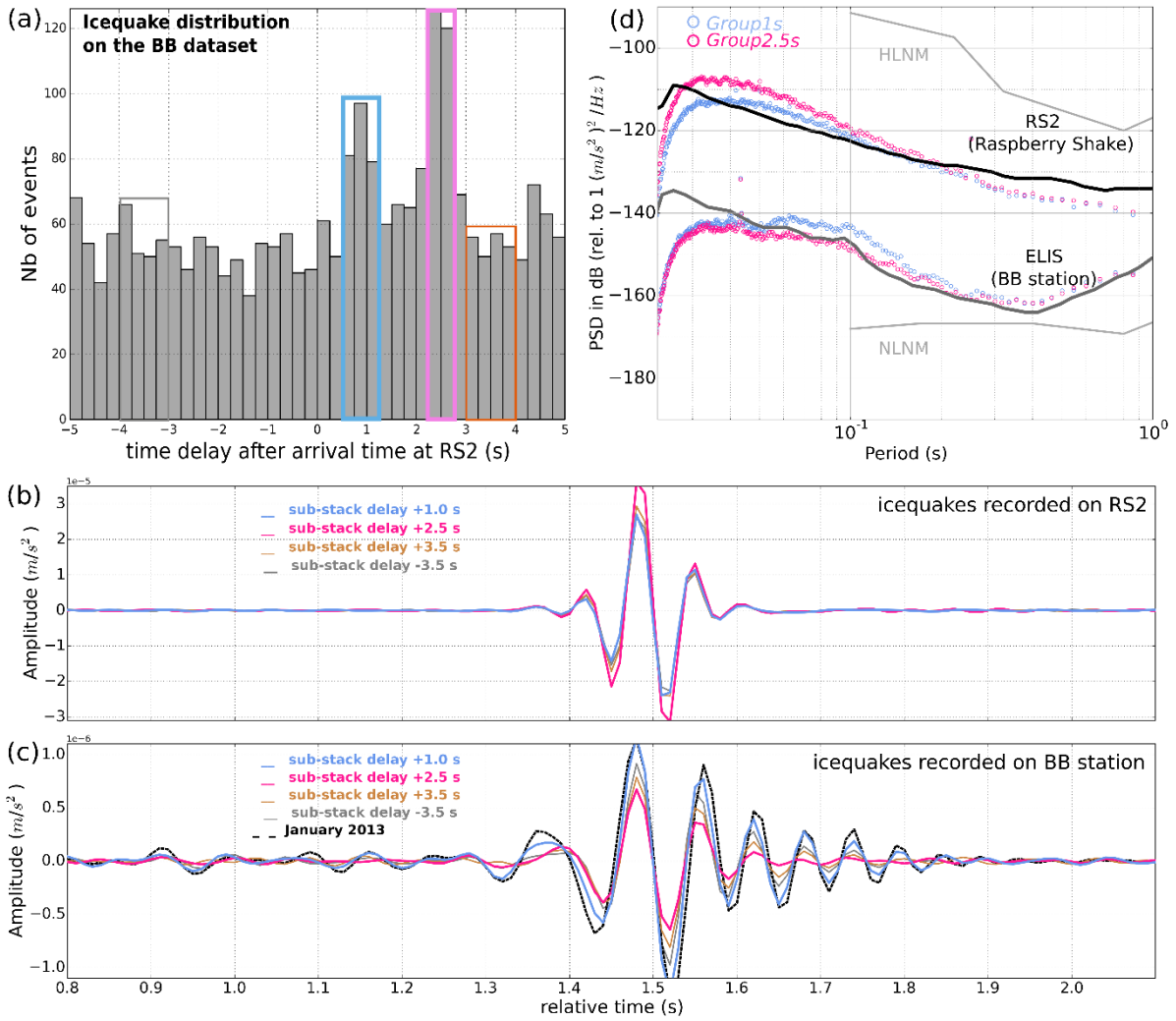
672

673 **Figure 3.** Icequakes recorded by RS2. (a) Cross-correlation plot of the 2936 icequake events
 674 detected at RS2; (b) stack trace of all recorded icequakes and the average signal (black line);
 675 (c) three component record of a typical icequake and (d) its frequency spectrum. Note that the
 676 horizontal components (EHN and EHE) were not synchronized with the BB data, and therefore
 677 their timing is unreliable.



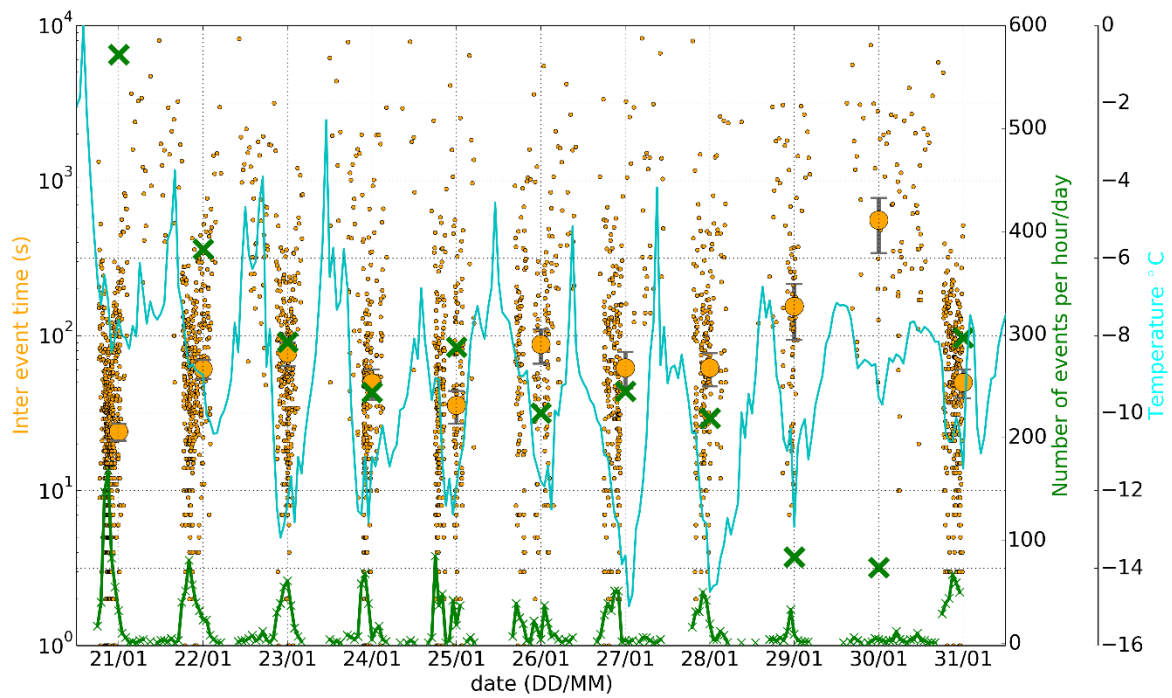
678

679 **Figure 4.** Five hundred individual traces randomly chosen from the 2936 seismic traces from
 680 (a) the BB data set and (b) the linear stack for the complete data set (solid line), with the
 681 standard deviation noted (b, gray lines). The seismic signal was band-pass filtered between 5
 682 and 20 Hz and aligned on the surface-wave largest peak (found by exploring ± 5 s around the
 683 arrival time at RS2). The stack trace from events detected by the same BB seismometer in
 684 January 2013 (Lombardi et al., 2019) is included for comparison (dashed line in b). This stack
 685 trace was normalized to match the largest amplitude of the stack trace from this study. Note
 686 that the P wave is not visible in the stack traces and the indicated timing is from Lombardi et
 687 al. (2019).



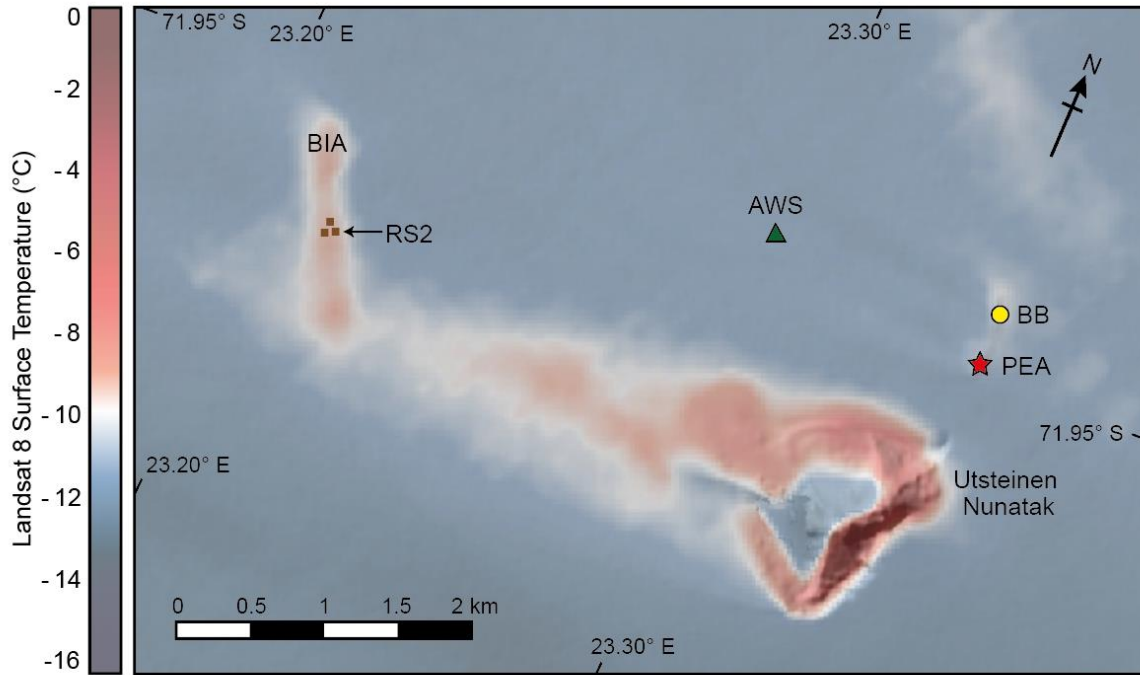
688

689 **Figure 5.** Distribution of seismic signals on the BB data set, based on detection from RS2. (a)
 690 Icequake distribution, presented in number of events, across the time delay—of the arrival time
 691 of the largest amplitude of the signal (within ± 5 s after the arrival time detected on RS2 data
 692 set). Note that the collected time delays are binned for every 0.25 s. Bins around 1 and 2.5 s
 693 (gathering more than 80 events) were selected as the largest bins. Bins representing the average
 694 number of events (around 50 events) are also shown for reference (bins -3.5 and +3.5 s). The
 695 colored boxes on (a) show the time delay of stacked seismic signals from the BB data set,
 696 displayed as a function of amplitude (meters per square second) in (d). (b) PSD of Group 1s and
 697 Group 2.5s are displayed on top of median PSD calculated over the 10-day monitoring period
 698 to show their importance relative to the background noise level. (c) Binned seismic signals on
 699 RS2.



700

701 **Figure 6.** Time history of the recorded events (small orange dots) in RS2, with the interevent
 702 spacing noted on the left y axis. Large orange circles with standard deviation bars show the
 703 average interevent time whereas large green crosses show the total number of events per day,
 704 corresponding to the right y axis in green. The small green crosses connected by green lines
 705 show the number of events per hour. Average air temperature (light blue line) recorded by the
 706 nearest AWS station is plotted on top. All events occur during times of minimum air
 707 temperatures, during the night period, between approximately 18:00 and 03:00 local time.



708

709 **Figure 7.** At sensor brightness measurements from the thermal infrared sensor (TIRS) onboard
 710 Landsat 8, collected across the field site during an orbital pass on 29 January, at 07:01 local
 711 time. The resultant surface temperature map (layered above a hillshade map) shows elevated
 712 surface temperature measurements around Utsteinen nunatak (which is largely free of snow
 713 and ice) and on wind-scoured surfaces west of the nunatak, including our study site, where BIA
 714 surface temperatures are approximately 3°C warmer than surrounding snow-covered ice during
 715 this early morning orbital pass. This suggests that BIAs could be more prone to larger
 716 fluctuations in surface temperature (due to differences in albedo and thermal insulation),
 717 generating increased surface expansion and contraction (as well as associated seismicity) in
 718 BIAs, compared to neighboring ice flows.